

NANOTECHNOLOGY IN BIOLOGY AND MEDICINE

Methods, Devices, and Applications

CRC Press
Taylor & Francis Group
6000 Broken Sound Parkway NW, Suite 300
Boca Raton, FL 33487-2742

© 2007 by Taylor & Francis Group, LLC
CRC Press is an imprint of Taylor & Francis Group, an Informa business

No claim to original U.S. Government works
Printed in the United States of America on acid-free paper
10 9 8 7 6 5 4 3 2 1

International Standard Book Number-10: 0-8493-2949-3 (Hardcover)
International Standard Book Number-13: 978-0-8493-2949-4 (Hardcover)

This book contains information obtained from authentic and highly regarded sources. Reprinted material is quoted with permission, and sources are indicated. A wide variety of references are listed. Reasonable efforts have been made to publish reliable data and information, but the author and the publisher cannot assume responsibility for the validity of all materials or for the consequences of their use.

No part of this book may be reprinted, reproduced, transmitted, or utilized in any form by any electronic, mechanical, or other means, now known or hereafter invented, including photocopying, microfilming, and recording, or in any information storage or retrieval system, without written permission from the publishers.

For permission to photocopy or use material electronically from this work, please access www.copyright.com (<http://www.copyright.com/>) or contact the Copyright Clearance Center, Inc. (CCC) 222 Rosewood Drive, Danvers, MA 01923, 978-750-8400. CCC is a not-for-profit organization that provides licenses and registration for a variety of users. For organizations that have been granted a photocopy license by the CCC, a separate system of payment has been arranged.

Trademark Notice: Product or corporate names may be trademarks or registered trademarks, and are used only for identification and explanation without intent to infringe.

Library of Congress Cataloging-in-Publication Data

Nanotechnology in biology and medicine : methods, devices, and applications / edited by Tuan Vo-Dinh.

p. ; cm.

Includes bibliographical references and index.

ISBN-13: 978-0-8493-2949-4 (hardcover : alk. paper)

ISBN-10: 0-8493-2949-3 (hardcover : alk. paper)

1. Nanotechnology. 2. Biomedical engineering. 3. Medical technology. I. Vo-Dinh, Tuan.

[DNLM: 1. Nanotechnology. 2. Biomedical Engineering--methods. QT 36.5 N186 2006]

R857.N34N36 2006

610.28--dc22

2006021439

Visit the Taylor & Francis Web site at
<http://www.taylorandfrancis.com>

and the CRC Press Web site at
<http://www.crcpress.com>

13

Three-Dimensional Aberration-Corrected Scanning Transmission Electron Microscopy for Biology

Niels de Jonge
Oak Ridge National Laboratory

Rachid Sougrat
National Institutes of Health

Diana B. Peckys
Oak Ridge National Laboratory

Andrew R. Lupini
Oak Ridge National Laboratory

Stephen J. Pennycook
Oak Ridge National Laboratory

Summary	13-1
13.1 Introduction.....	13-2
13.2 Overview of High-Resolution 3D Imaging Techniques for Biology	13-3
Confocal Laser Microscopy • X-Ray, NMR, and Other • Electron Tomography	
13.3 From the First STEM to Aberration Correction	13-6
The First STEM • The STEM Imaging with Several Parallel Detector Signals • Reciprocity • Phase Contrast versus Scatter Contrast • Aberration-Corrected STEM • 3D STEM	
13.4 Resolution of 3D STEM on Biological Samples.....	13-12
Radiation Dose • Blur • Scatter Contrast • Detection of an Embedded Staining Particle • Confidence Level of Detection • Dose-Limited Resolution • Dose-Limited Resolution in Focal Series	
13.5 Initial Experimental Results on a Biological Sample....	13-18
Focal Series of a Conventional Thin Section • Deconvolution • Deconvolved Images	
13.6 Future Outlook.....	13-20
13.7 Comparison of 3D STEM with TEM Tomography for Biology.....	13-21
13.8 Conclusions.....	13-21

Summary

Recent instrumental developments have enabled greatly improved resolution of scanning transmission electron microscopes (STEM) through aberration correction. An additional and previously unanticipated advantage of aberration correction is the largely improved depth sensitivity that has led to the reconstruction of a three-dimensional (3D) image from a focal series.

In this chapter the potential of aberration-corrected 3D STEM to provide major improvements in the imaging capabilities for biological samples will be discussed. This chapter contains a brief overview of

the various high-resolution 3D imaging techniques, a historical perspective of the development of STEM, first estimates of the dose-limited axial and lateral resolution on biological samples and initial experiments on stained thin sections.

13.1 Introduction

With the 2.91 billion base pairs of the human genome mapped [1–3], one of the main challenges facing science is to understand the functioning of more than 26,000 encoded proteins. For the overwhelming majority of proteins it is not well understood why a certain amino acid sequence leads to a specific tertiary structure into which the protein folds [4]. Only for very small molecules it is possible to numerically calculate their folding in a reliable manner. Our true mastery of self-assembly is therefore limited to relatively simple systems [5–7]. Many questions remain open concerning the highly complex organization of the proteins into functional cells. The limited comprehension of protein and cell function is mainly due to a lack of detailed structural information [4,8]. To date only about 90 unique structures of membrane proteins have been resolved [4]. Moreover, the organization of proteins in cells has only been accessible so far by techniques that do not combine high spatial resolution with imaging in their native environment, or the imaging of dynamical behavior.

Ideally, one would like to have access to an imaging technique providing the eight requirements listed in Table 13.1. Only such a technique allows a direct, *in vivo*, study of the function of the molecular machinery. Of secondary importance, but in many cases a limiting factor is obviously the cost of the apparatus and its operation. Figure 13.1 schematically presents the fulfillment of the eight main requirements versus the resolution of the technique. A trend exists in which better resolution can be achieved only at the cost of less direct imaging of the functioning of the cell, subunit, or protein.

Figure 13.1 illustrates that a clear need and drive exists to push existing techniques and develop new techniques that provide high-resolution imaging with as close to *in vivo* capabilities as possible. At a resolution below 1 nm already much can be gained when only four or five requirements are met, whereas in the region of a few to several tens of nanometers resolution seven requirements can be met. Electron microscopy (EM) techniques based on averaging over many images of a single type of particle continue to push the limit on the high-resolution side [9], whereas on the tens of nanometers side confocal laser microscopy is gaining ground [10].

Recent instrumental developments have enabled drastic improvements in the resolution of STEM using aberration correction [11]. An additional and previously unanticipated advantage of aberration correction is the greatly improved depth sensitivity that has led to the reconstruction of a 3D image from a focal series [12,13]. In this chapter we will discuss the potential of aberration-corrected 3D STEM to

TABLE 13.1 Requirements for the Imaging of Biological Function in Addition to High Resolution

Number	Requirement
1	3D imaging
2	In natural liquid environment, i.e., not frozen
3	Single particles, i.e., no crystals
4	The whole assembly comprising, for example, many proteins reacting together, or a whole protein complex and not only small subunits
5	Time-resolved
6	Intracellular, not only surface
7	Reproducibility
8	Fast imaging

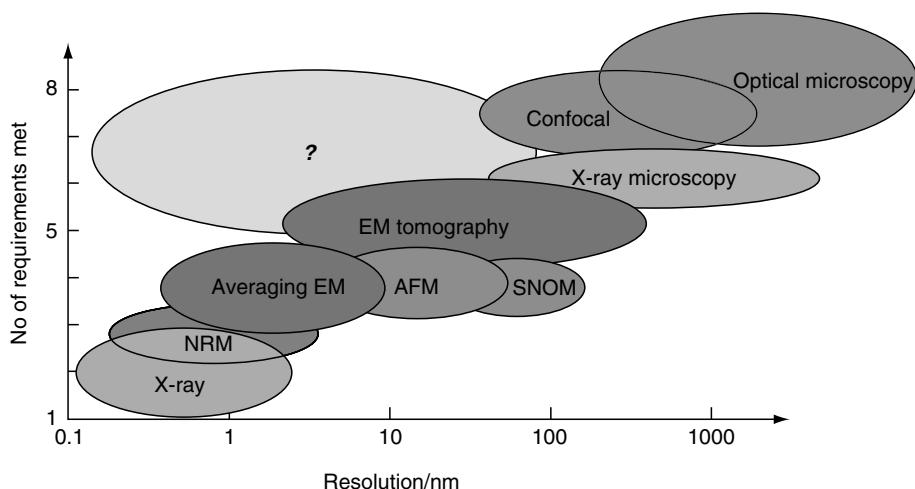


FIGURE 13.1 Number of fulfilled requirements for the imaging of the functioning cell, or subunit *in vivo* versus the resolution for various imaging techniques. EM tomography means electron microscopy tomography. The figure is meant as guide for the discussion and by no means claims absolute limits of a certain technique. The ellipse with the question mark indicates the specifications of the ideal technique.

provide major improvements in the imaging capabilities for biological samples. First, we will give a brief overview of the different high-resolution 3D techniques and then we will introduce the reader to some of the history of EM, STEM, and aberration correction. In Section 13.3.6 the concept of 3D STEM will be described. Sections 13.4–13.5 will evaluate the potential of 3D STEM for high-resolution 3D imaging of stained biological samples.

13.2 Overview of High-Resolution 3D Imaging Techniques for Biology

13.2.1 Confocal Laser Microscopy

Confocal laser microscopy is one of the most versatile techniques for 3D imaging currently available, but, based on light, runs into resolution limits the soonest. Confocal laser microscopy is a light optical 3D technique for imaging biological samples with a lateral and axial resolution of 0.15 and 0.46 μm , respectively, under optimal conditions [14,15]. This technique has some major advantages. Samples can be imaged in their buffer solution under fully native conditions and at room temperature. The confocal laser microscope can also be used to image dynamic processes with time. True cell functioning can thus be imaged *in vivo*, for example, in response to certain stimuli [16]. In some cases the resolution can be improved by deconvolution [17]. Recently, it has even been shown that Abbe's diffraction limit of resolution [18] can be broken by special nonlinear techniques, such as the 4- π microscope [19] or by stimulated emission depletion [10]. It is expected that these far-field techniques will be improved soon resulting in 3D optical images with a resolution of perhaps only several tens of nanometers on fluorescent particles.

13.2.2 X-Ray, NMR, and Other

X-ray crystallography can determine the atomic structures of huge proteins when high-quality crystals can be obtained, for example the photosynthetic reactor center [20] (see Figure 13.2). A major disadvantage is the time-consuming process of producing high-quality crystals. Moreover, many proteins, especially, membrane proteins do not crystallize. Crystal structures do not necessarily or always

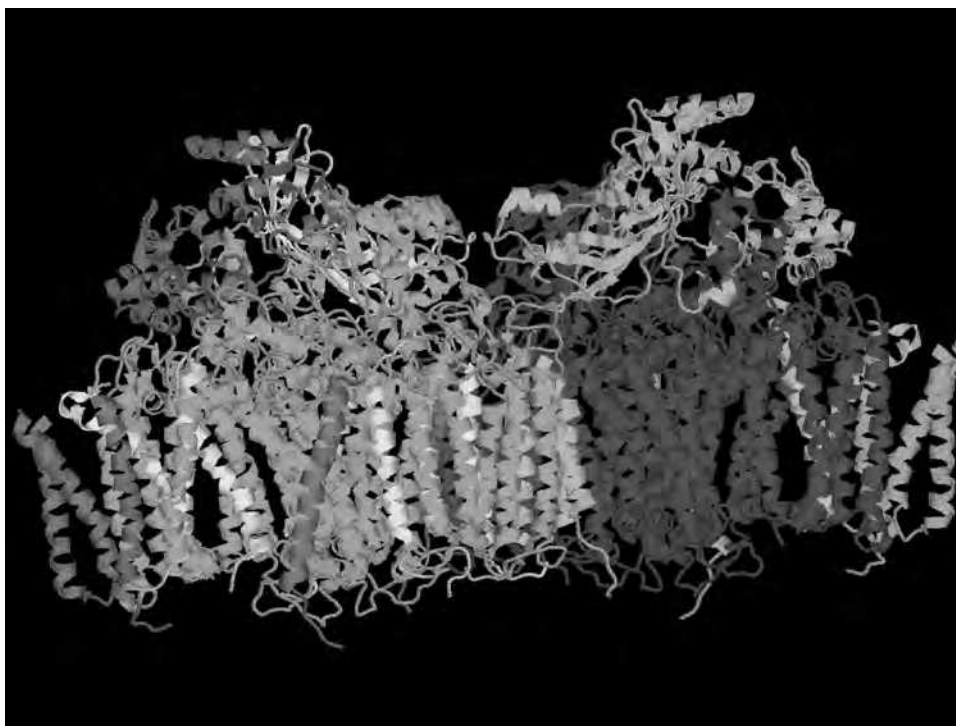


FIGURE 13.2 (See color insert following page 18-18.) Photosystem II crystal structure obtained from the PDB database, entry 1s5l. PSII is the membrane protein complex found in oxygenic photosynthetic organisms (higher plants, green algae, and cyanobacteria), which collects light energy to split H_2O into O_2 , protons, and electrons. It is responsible for the production of atmospheric oxygen, essential for aerobic life on this planet.

resemble the native state of the protein. The function of proteins is often related to structural changes, requiring the crystallization of many different conformations.

NMR spectroscopy can also be used to obtain atomic 3D information, but can only be applied for small molecules. The calculated structure cannot always be determined unambiguously and a set of solutions may be given. Recent developments are in the direction of resolving larger structures up to 900 kDa [21].

Note that these techniques are not imaging techniques but structure determination methods. They assume that the structure is perfectly repeated and give an average structure as opposed to a direct real space image. It is worth mentioning that several other techniques exist, but are not yet used as standard tools for structural biology, for example, neutron scattering [22], x-ray microscopy [23] and atomic force microscopy [24]. In particular, AFM can be of potential benefit as it allows high-resolution imaging of surfaces of biological samples under native (in water) conditions as demonstrated, for example in the imaging of the photosynthetic membranes [24].

13.2.3 Electron Tomography

In electron tomography 3D images can be reconstructed from images of an object recorded at several tilt angles. These images can be obtained by either mechanically tilting the sample stage [25,26], or by recording images of a sample containing many identical objects randomly oriented [9,27]. A 3D reconstruction is then obtained by using tomography. The first successful reconstructions were already published over 30 years ago [28,29]. Aaron Klug was awarded the Nobel Prize for his work in structural biology [30].

Various sample preparation methods exist. Conventional techniques for the preparation of biological samples imply a fixation step using aldehydes then a dehydration followed by the infiltration of the specimen by a resin. The preparation is stained with heavy metals (osmium or uranyl acetate) and may be contrasted by lead [31]. Most recent techniques (cryoelectron microscopy or cryo-EM) use cryo-fixation: the sample is immobilized by ultra-rapid freezing. Thus the preparation is embedded in vitreous ice. No stain is added and the true density is visualized [32]. Several other methods exist, such as the combination of negative staining and cryo-EM [33] and rapid freezing and freeze substitution [25].

EM is often considered as the fastest technique to visualize single protein complexes because it does not require protein crystals. However, the resolution is limited and specimen-related [34,35]. Cryo-EM of unstained samples is mainly limited by radiation damage, whereas the harsh treatment used in the conventional EM limits the capability of imaging biological material in their native state. For thin samples other important limiting factors are: (1) signal-to-noise ratio in the image, (2) the drift of the stage, (3) defocus variation through the field of view, and (4) the missing information due to the missing wedge (or cone). In tilt-series transmission electron microscopy (TEM) the best obtainable resolution is 3 nm at a dose of $20\text{--}80\text{ e}^{-}/\text{\AA}^2$; often the resolution is worse (5–20 nm) and the resolution determination itself is not trivial [26,36–40]. For samples thicker than 100–200 nm other limiting factors are beam blurring and defocusing effects, which can be partly solved by energy filtering [41–43] and through the use of high voltages. Examples of 3D reconstructions obtained with tilt-series TEM are those of muscle actinin [44], the work on the Golgi complex (see Figure 13.3) [45], the structure of the nuclear pore complex [46], and the visualization of the architecture of a eukaryotic cell [41].

In single-particle tomography, a large number of images are recorded containing images of the object under various projection angles. The particles are selected and aligned in an automated procedure. A 3D reconstruction is then obtained from the average image of the object [9,27]. This technique has two

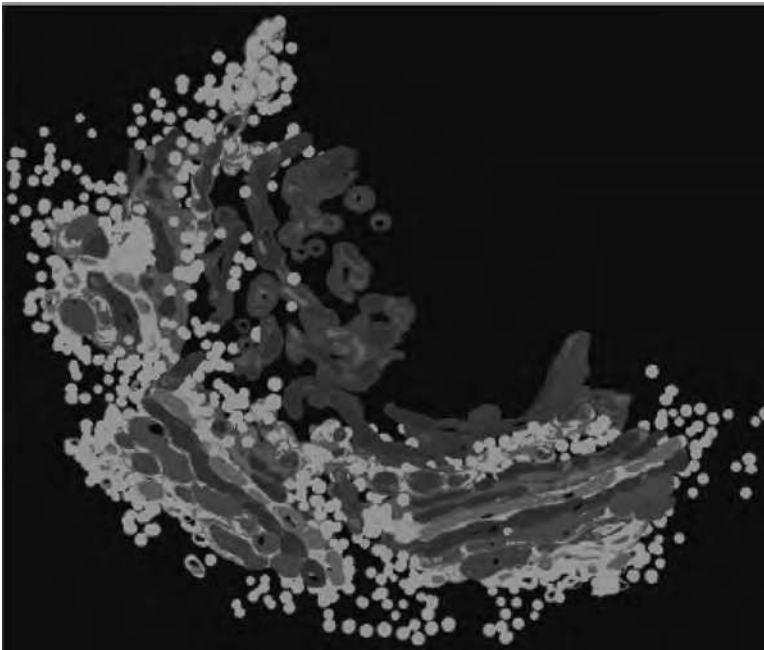


FIGURE 13.3 3D reconstruction of the Golgi ribbon. (From Mogelsvang et al., *Traffic*, 5, 338, 2004. With permission.)

major advantages: (1) a much lower dose ($<10\text{ e}^-/\text{\AA}^2$) can be used in the imaging of unstained samples, such that the images likely present the object more closely to its native state, (2) this technique provides a subnanometer resolution. The main drawback is that a sample has to be prepared containing many similar objects, e.g., proteins, viruses, and microtubules, thus preventing imaging whole assemblies. Furthermore, the assumption is made that all objects have exactly the same shape, which obviously might not always be the case. Often images with higher resolution are obtained with objects that contain a certain degree of symmetry. Some examples of resolved structures of purified proteins are those of bacteriorhodopsin [47] with a lateral resolution of 3.5 \AA , that of the aquaporin at 3.8 \AA resolution [48], the plant light-harvesting complex at 3.4 \AA [49] and at a somewhat lower axial resolution, the structure of the calcium pump [50] and the microtubule structure [51], both at 8 \AA . Single particle EM is used frequently to image the structures of viruses [52,53]. In some cases electron crystallography is used as an alternative 3D technique in cases where large crystals for x-ray crystallography cannot be obtained [49].

13.3 From the First STEM to Aberration Correction

13.3.1 The First STEM

The first electron microscope was developed by Ernst Ruska in the early 1930s in Berlin [54,55] for which he was awarded the Nobel Prize in 1986 [56]. His younger brother Helmut Ruska who had a medical background recognized the potential importance of the new microscope for biology [57] and in 1938 Siemens established a special laboratory for electron microscopy in close collaboration with both brothers, see Figure 13.4. The first STEM was built in 1938 by von Ardenne [58]. At that time the instrument was limited by the low brightness of the electron source and did not have advantages over the TEM. It would take another 30 years before a high-brightness field emission electron source was developed that led to the construction of the first high-resolution STEM by Crewe in Chicago, which was the first electron microscope to image single atoms [59] and was soon considered important in the field of biology [60]. It is remarkable that the development of the STEM was for so long limited by the lack of a good electron source, when Fowler and Nordheim had already described the fundamentals of field emission in 1928 in Berlin [61] and several scientists had worked on the subject from the 1930s on. Mueller had, for example, worked on electron sources and ion sources in Berlin already in the 1930s. His work finally led to the development of the field ion microscope, which produced the first images of single atoms. For an overview see Good and Mueller [62].

13.3.2 The STEM Imaging with Several Parallel Detector Signals

Following the introduction of the high-brightness field emission STEM, the advantage of multiple detectors, see Figure 13.5, was soon appreciated. As the image-forming lens is before the specimen, it is particularly straightforward to separate three distinct classes of electron detection [63]: (1) elastic scattering leads to large angles of scattering, and an annular dark field (ADF) detector can collect a large fraction of the total elastic scattering. Inelastic scattering is predominantly forward peaked and passes through the hole in the ADF detector. It is simple therefore to collect simultaneously either (2) a bright field (BF) image, or by passing the transmitted beam through, and (3) a spectrometer, an inelastic image, and electron energy loss spectroscopy (EELS). The ADF image is approximately the complement of the BF image (for a large BF detector) in STEM, therefore, which detector receives the most electrons depends on the projected mass density of the area that is imaged. For weakly scattering objects, the ADF image is preferable because the image sits on a weak background whereas the BF image is on a high background, with consequent high noise [64]. Spectacular images of individual atoms, stained DNA, and biological macromolecules were rapidly obtained [63,65]. 3D reconstructions were

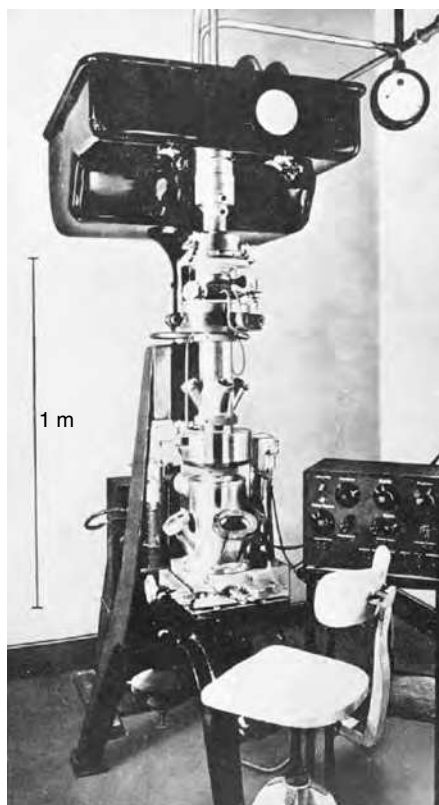


FIGURE 13.4 Preserial high-resolution electron microscope (1938). (From Kruger, D.H., Schneck, P., and Gelderblom, H.R., *Lancet*, 355, 1713, 2000. With permission.)

made through combining data from a set of dark field images [66–68], and STEM tomography was recently implemented [69,70].

The signals from the different detectors can also be combined; the original *Z*-contrast mode (where *Z* is atomic number) was obtained by taking the ratio of the elastic signal to the inelastic signal [59]. This effect can be used in biology to image high-*Z* atoms in a protein matrix, as was shown for ferritin [71] and it can be used to image specific gold labels in biological sections [72]. For materials science applications a high-angle ADF detector is used to suppress coherent diffraction contrast [73,74].

Image averaging techniques were introduced extending the range of visibility of single atoms down to sulfur [75,76]. Detailed analysis of the trade off between image contrast and radiation damage was undertaken [71,76,77]. More rigorous calculations of scattering cross sections [78], led to quantitative means for determining molecular weights [79–81], and to an optimized combination of the different detector signals to eliminate the effect of variation of the sample thickness in the field of view of an image [82]. Several STEMs are equipped with an EELS [60] that are used to investigate the inelastic scattering at low angles, for example, to reduce effects of sample thickness variations [43,83]. EELS has been widely used in materials science to provide chemical information of the sample with atomic resolution by recording simultaneous signals for all detectors [84,85].

13.3.3 Reciprocity

In parallel with the applications to biology was an analysis of the image contrast mechanism in TEM and STEM [86–88]. The contrast mechanisms are explained in detail in several books, e.g., those of Reimer

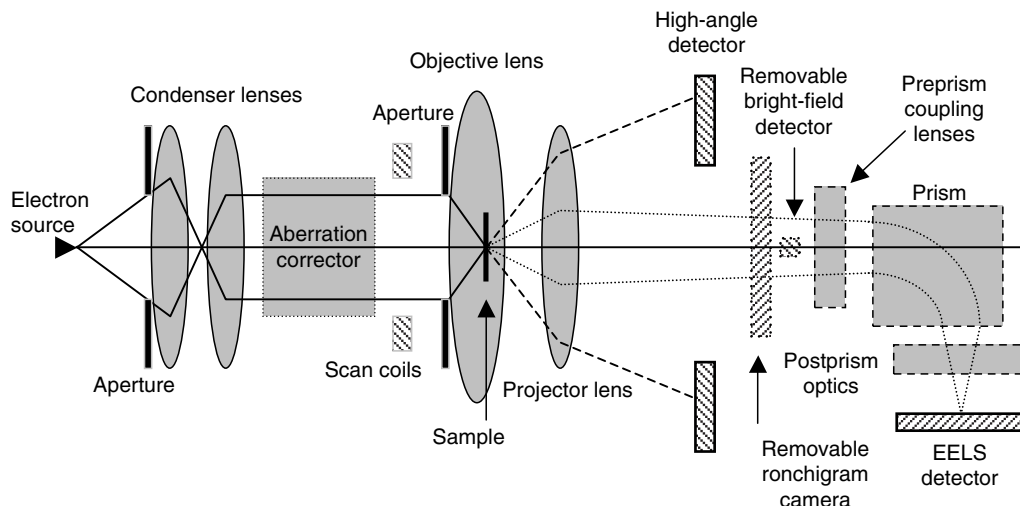


FIGURE 13.5 Schematic drawing of a scanning transmission electron microscope (STEM) equipped with an aberration corrector. Electron trajectories at the edge of the apertures are indicated with solid lines. High-angle scattering used to form the Z-contrast image is indicated with dashed lines and low-angle scattering directed toward the EELS is indicated with dotted lines.

[89] and Spence [90]. It was established that because elastic scattering is the dominant form of image contrast, which is independent on the direction of beam propagation, the principle of reciprocity should apply, and BF STEM and TEM should give the same image contrast. (Specifically, the STEM detector should be the same angular size as the TEM condenser aperture, and the two objective apertures should also be equal. Also, the STEM objective aperture should be filled coherently and the TEM condenser aperture should be filled incoherently.) The first BF STEM images with a small collector aperture indeed showed phase contrast effects typical of TEM imaging, crystal lattice fringes, and the speckle pattern of amorphous carbon [60]. Historically, however, phase contrast imaging in STEM has been too noisy to be useful even for damage-resistant materials, until the introduction of the aberration corrector. On the other hand, ADF STEM has always been a relatively efficient mode of imaging, but the reciprocal arrangement, a very wide angular illumination (or hollow cone) could not be reproduced in the TEM. For many years the two microscopes developed on separate paths and reciprocity was just a theoretical connection.

13.3.4 Phase Contrast versus Scatter Contrast

High-resolution TEM imaging mostly uses phase contrast, whereas STEM mostly uses scatter contrast. Each contrast mechanism has its advantages and disadvantages. Phase contrast imaging in TEM is a highly efficient way to image weakly scattering objects and used mostly on unstained samples [25]. This is because it is based on the interference of amplitudes, and changes in the amplitude of the transmitted beam are converted directly into intensity changes. If sensitivity is the advantage of phase contrast imaging, interpretability is the penalty. For example, single heavy atoms on a thin film of amorphous carbon are not visible in phase contrast imaging because they are obscured by the strong coherent speckle pattern from the amorphous carbon. They are only observable if the support is a crystal, and the crystal spots are excluded from forming the image [91]. A second disadvantage is that phase contrast imaging is more efficient at high resolution. Phase contrast imaging uses the lens aberrations to rotate the phase of the scattered beam by (ideally) 90° so that it will interfere with the transmitted beam amplitude. Low-resolution information is carried by electrons scattered through low angles, where the lens aberrations are small. For imaging materials with spacings in the range $2\text{--}3 \text{ \AA}$ phase contrast is very

effective but for resolutions in the biological regime above 3 Å it becomes progressively less sensitive [92] and very large defocus values are needed of several hundreds of nanometers to tens of micrometers [27,41]. Recently the successful construction of a phase plate has been reported that may overcome this limitation [93]. Third, in phase contrast microscopy, the contrast depends on the relative phases between the scattered and the unscattered beams, which can be constructive or destructive. The relative phases depend not only on the angle of the scattered beams but also on the objective lens defocus and the specimen thickness, in a complex manner, i.e., the images are difficult to interpret. Fourth, phase contrast is very sensitive to inelastic scattering, which is problematic especially for thick samples. High-quality images of biological samples are, therefore, sometimes recorded using an image energy filter, such that only elastically scattered electrons are used to form an image [41–43].

The initial scatter contrast images of single atoms and clusters by Crewe and coworkers [65], as well as image simulations [87] showed the clear signature characteristics of an incoherent image, a single unique focus for the atoms and a resolution that is approximately $\sqrt{2}$ better than phase contrast imaging. Also the images demonstrated increased Z -contrast, i.e., a stronger contrast as function of Z , as expected, since high angle scattering approaches the cross section for unscreened Rutherford scattering, which is proportional to Z^2 . Scatter contrast can be thought of as a convolution between the object scattering power and the probe intensity profile. Due to this simple and direct relationship between the object and image, the image can be interpreted directly, even in an analytical way, such that molecular weights can be determined [80] and crystal structures can be determined with atomic resolution [94–96]. Surprisingly, the images of crystals also show exactly the characteristics expected for an incoherent image, a single unique focus and a simple dependence on sample thickness with no contrast reversals in either case.

The quantum-mechanical explanation [96] for the very different images obtained from incoherent, or coherent imaging given the same incident probe is that the high-angle detector is only sensitive to the electron wave function near the atomic sites, where the scattering is incoherent. The phase contrast image uses the coherent part of the emergent electron wave function, and therefore gives an image with coherent character.

13.3.5 Aberration-Corrected STEM

The resolution of a state-of-the-art high voltage STEM is determined by the optimal balance between the diffraction and the spherical aberration of the objective lens (spherical aberration causes electrons traveling at higher angles to the optical axis to be focused too strongly). For the 300 kV VG STEM at ORNL the d_{50} spot size containing 50% of the current amounts to 1.9 Å for a beam opening semiangle of 9 mrad as optimized for small beam tails. The resolution of the imaging depends also on the sample and can in some cases be optimized at the Scherzer defocus allowing for somewhat larger beam tails. Lens aberrations cannot be corrected for with a combination of positive and negative lenses, as is the case for light optics using round lenses. This was already proved in 1936 by Scherzer for the case of rotationally symmetric lenses with a constant field and no charge on axis [97]. Scherzer [98] proposed in 1947 to correct lens aberrations by breaking the rotational symmetry, using nonround elements, known as multipoles, placed close to the objective lens. Multipoles are named after their rotational symmetry: dipoles, quadrupoles, sextupoles (or hexapoles), octupoles, and so on. Despite many attempts only very recently working correctors were realized that actually improved the resolution in a high-end microscope [99,100].

Two types of aberration correctors exist, both of which have a long history [101–103]; the quadrupole–octupole corrector [100,104] and the round lens–hexapole corrector [99,105–107]. In a quadrupole–octupole corrector, the octupoles provide the fields to correct the spherical aberration and the quadrupoles form the beam into the right shape at the positions of the octupoles. After correction, the resolution is mainly limited by the fifth-order spherical aberration C_5 . In a hexapole corrector [105,106] the extended hexapoles correct C_5 and pairs of round lenses are used to project the beam from one hexapole to the other and into the objective lens. This type of corrector can be relatively simple, but still have good high-order aberrations [108].

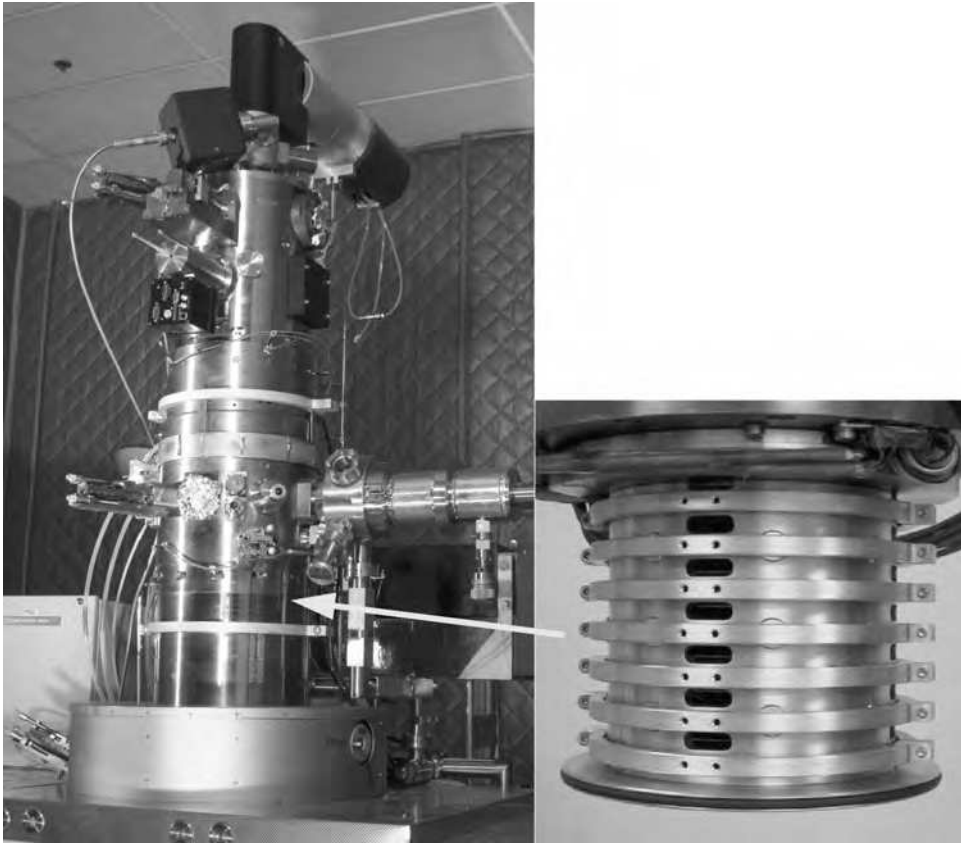


FIGURE 13.6 The 300 kV STEM at ORNL with aberration corrector (right inset).

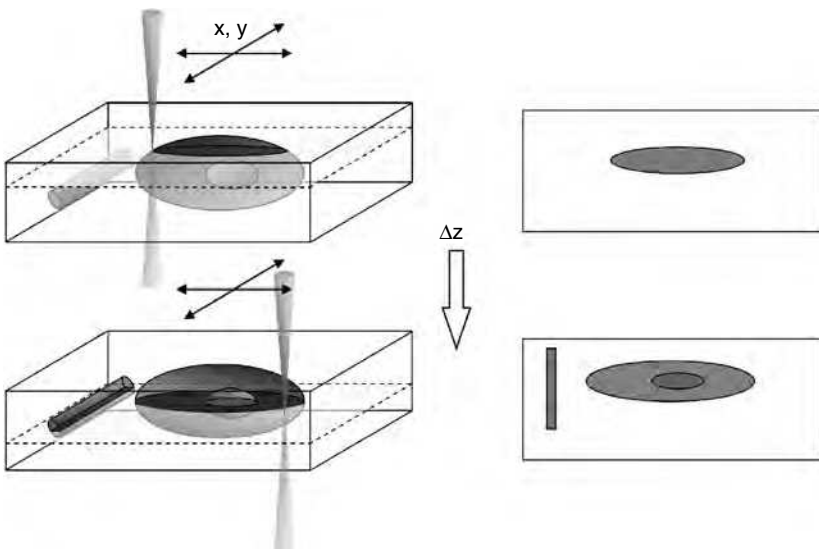


FIGURE 13.7 Principle of operation of 3D STEM (left). The electron beam scans in x and y direction over the objects contained in a thin section at a certain focal depth, forming one image. Successively the focus is changed and a new image is recorded. This process is repeated to obtain a 3D data-set (right). Each 2D image represents a slice of the 3D data-set.

Limiting factors were (1) the extreme required mechanical precision of the multipole elements, (2) the required stability of the power supplies (better than 1 ppm), and 3) the alignment procedure. Practical use of the correctors in science was only possible after automated procedures to measure the aberrations and set the over 40 power supplies using modern computers [100,104,109].

Developments at ORNL using a NION aberration corrector in a VG microscopes HB603U, see Figure 13.6, STEM at 300 kV equipped with a cold field emission gun led to the world record of resolution with a spot diameter of approximately 0.8 \AA , $\alpha = 23 \text{ mrad}$, and an information limit of 0.6 \AA [11]. The second generation of correctors, with full correction of C_5 will lead to even better values of the resolution [110] as low as 0.4 \AA with opening angles as large as 50 mrad. The improved signal-to-noise ratio when imaging with the aberration-corrected probe, which is significantly sharper than uncorrected, provides much better contrast and sensitivity for single atom detection.

13.3.6 3D STEM

Probe convergence angles in aberration-corrected STEM are sufficiently large that the depth of focus becomes less than the sample thickness. This effect can be used to obtain depth sensitivity. The technique collects information in a similar way as in confocal microscopy. The sample is scanned with a beam layer-for-layer, as shown in Figure 13.7. Recently, it was demonstrated that 3D images could be reconstructed from focus series with atomic lateral resolution [12,13] (see, for example, Figure 13.8).

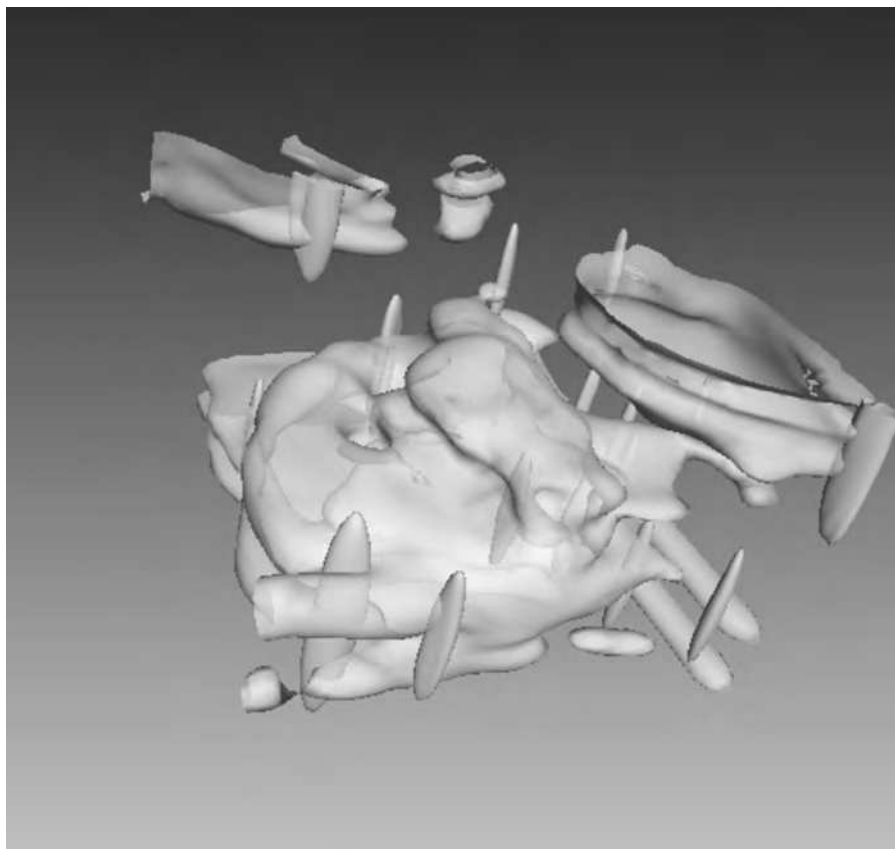


FIGURE 13.8 3D rendering of a sample with a Pt, Au catalyst (vertical silver-like structures), embedded in a TiO_2 substrate. (From Borisevich et al., *Proc. Natl. Acad. Sci.*, 103, 3044, 2006. With permission.)

Using the electron optical analog of the Raleigh criterion, it was shown that the axial resolution obeys the following equation [13]:

$$dz \approx \frac{2\lambda}{\alpha^2} \quad (13.1)$$

For the aberration-corrected beam of the VG 603 at ORNL the wavelength of the electron $\lambda = 1.97$ pm, the beam semi-angle $\alpha = 23$ mrad, and thus the incoherent depth resolution is $dz = 7.4$ nm. This number corresponds with experimental data on platinum atoms on a thin carbon support [13]. Note that the depth precision to determine the axial position of well separated point-like objects can be much better than the axial resolution. It was indeed shown on hafnium atoms in a silicon oxide layer that the depth precision was better than 1 nm [12]. The depth resolution is much better than that of a state-of-the-art STEM at 300 keV without corrector operating at $\theta = 9$ mrad, such that $dz = 49$ nm. Commercial TEMs used for biological samples are often operated at even smaller opening angles leading to values of the focal depth of typically 100 nm.

The 3D STEM is not a true confocal microscope, as it does not have a pinhole aperture. 3D reconstruction involves deconvolution of the image, as in wide-field microscopy [14,17]. The idea of a true confocal electron microscopy was proposed by Zaluzec [111]. However, this concept involves some major practical difficulties due to the need for a high-precision synchronous de-scan to map the beam on the pinhole aperture. The electron optical variant of a 3D wide-field microscope was originally introduced by Hoppe in 1972, but soon abandoned due to practical difficulties [112].

13.4 Resolution of 3D STEM on Biological Samples

The high resolution obtained on the highly scattering materials embedded in solid matrices cannot be achieved with biological materials. Imaging biological materials involves low Z elements (H,C,N,O) in a matrix of amorphous ice for unstained cryo samples, or polymer for embedded samples. Conventional stained sections contain a high Z material, for example, osmium, in a polymer matrix. Radiation damage is the main limiting factor in the imaging of biological or polymer samples. Secondly, the samples of interest have a large thickness (100–500 nm) compared with the typically ultra-thin samples used in materials science (10–50 nm). The resolution might therefore be decreased by beam blurring. To evaluate the use of 3D STEM for biology, we have to calculate the expected resolution taking into account the radiation damage and the beam blurring. In this section, we will calculate the resolution for osmium stained and epoxy embedded conventional thin sections for a thickness where the beam blurring can be neglected.

13.4.1 Radiation Dose

The amount of signal that can be obtained from a sample is limited by the maximal radiation dose that the sample accumulates [89,113,114]. Dose limits of organic materials depend on the chemical composition and on the electron beam energy. Typically, aliphatic materials allow a smaller dose than the compounds with aromatic rings. The radiation damage has several mechanisms. Beam damage from reversible processes such as heating, charging, and the formation of radicals depend on the flux of electrons and will, consequently, depend on the way the sample is imaged, for example, applying the same electron dose for a longer period of time will lead to less damage than the same dose applied for a shorter period of time. We refer to this sort of damage by type I. Irreversible processes, i.e., type II damage, on the other hand, are independent of time and depends only on the total number of electrons

applied, no matter in which way. Examples of type II processes are the breaking of bonds and several types of structural rearrangements.

Conventional sections consist of a mixture of polymers, with aromatic compounds to reduce the beam damage. Such a polymer, for example, poly(ethylene terephthalate) has a critical dose of typically $2 \times 10^2 \text{ e}^-/\text{\AA}^2$ at 100 keV, measured by the vanishing of the EELS signal [82,89,114,115]. This value is close to the limit of $80 \text{ e}^-/\text{\AA}^2$ in TEM cryotomography at 300 keV of vitrified samples at liquid nitrogen temperature [36–39]. The maximal dose that can be used for the imaging of a stained and epoxy embedded sample is much larger. In a typical experiment the sample is pre-irradiated with a dose of approximately $1 \times 10^2 \text{ e}^-/\text{\AA}^2$ leading to a rapid shrinkage of the sample to about 80% of its original thickness and 90% of its lateral dimension, followed by a long period with relative stability of the sample. Imaging times of half an hour are not uncommon at low magnifications and the total dose can amount up to $4 \times 10^3 \text{ e}^-/\text{\AA}^2$ for an Araldite [116] section of 80 nm thickness [117]. Others perform high-resolution imaging for a dose up to $1 \times 10^3 \text{ e}^-/\text{\AA}^2$ [40]. In this study we will use a maximal dose of $4 \times 10^3 \text{ e}^-/\text{\AA}^2$.

13.4.2 Blur

An important issue is the effect of beam scattering by the sample occurring when the beam passes through a sample of a certain thickness. Scattering decreases the signal-to-noise ratio and leads to beam broadening. Several models exist to evaluate the broadening effect analytically [118], but for very thin samples it is more accurate to perform Monte-Carlo simulations of the electron trajectories [120]. The equivalent spot diameter in the focal plane, d_{blur} , was calculated, using a parameterized Mott cross section, see Figure 13.9. The calculations were performed for Epon, assuming that the volume occupied by staining particles is only a small fraction of the total volume and can be neglected. It can be seen that for sections with a thickness up to 90 nm the effect of beam scattering is very small. For very thin foils a significant fraction of the beam is unscattered, resulting in a fully focused probe surrounded by a small “skirt” of scattered electrons. For sections thicker than 90 nm the final spot size d_{total} can be obtained from $d_{\text{total}} = \text{sqrt}(d^2 + d_{\text{blur}}^2)$ [120]. A complicating factor is that the diameter of the spot varies with the position of the spot in the section, i.e., the point spread function (PSF) varies with depth in the sample. The following calculations will be restricted to the simple case of a thin section for which beam broadening can be neglected, i.e., for $T = 90 \text{ nm}$, such that we can assume the free space probe parameters will apply, at least approximately.

13.4.3 Scatter Contrast

For high-resolution aberration-corrected STEM with depth sensitivity the ADF detector is used with an opening semiangle β that is larger than the beam opening semiangle α . The contrast mechanism is scatter contrast. When the beam interacts with a certain volume of a certain material, a certain fraction of electrons is scattered with an angle larger than β . The fraction of the electron beam scattered into the detector can be calculated [89] using the partial cross section for elastic scattering $\sigma(\beta)$. The fraction of electrons N/N_0 of an electron beam that is scattered with an angle larger than a

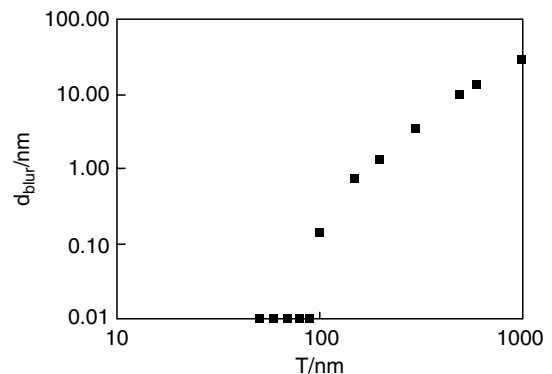


FIGURE 13.9 The diameter d_{blur} of the equivalent spot in the focal plane of beam broadening of an electron beam propagating through an Epon sample with thickness T at 300 KeV beam energy. The data-points represent results from a Monte-Carlo simulation, with each point obtained from 100000 rays. The diameter represents the full width at half maximum.

certain angle β when passing through a material with thickness z is given by:

$$\frac{N}{N_0} = 1 - \exp(-z\sigma(\beta)\rho N_A/W) = 1 - \exp\left(-\frac{z}{l}\right) \quad (13.2)$$

with Avogadro's number N_A , the atomic weight W , the density ρ , and the mean free path length l . The scattering cross section can be estimated by integration of the differential cross section $d\sigma/d\Omega$ assuming a simple screened Rutherford scattering model based on a Wentzel potential, which leads to the expression [89]:

$$\sigma(\beta) = \frac{Z^2 R^2 \lambda^2 (1 + E/E_0)^2}{\pi a_H^2} \frac{1}{1 + (\beta/\theta_0)^2} \quad (13.3)$$

Here a_H is the Bohr radius. Furthermore,

$$E_0 = m_0 c^2; \quad \lambda = \frac{hc}{\sqrt{2EE_0 + E^2}}; \quad \theta_0 = \frac{\lambda}{2\pi R}; \quad R = a_H Z^{-1/3} \quad (13.4)$$

With $E = Ue$, U the beam energy (keV) the electron acceleration voltage (v), m_0 the rest mass of the electron, c the speed of light, h Planck's constant, and e the electron charge. These equations give the values of the mean free path length for one element. For an ADF detector with $\beta = 30$ mrad and for the thin samples typically used for high-resolution 3D imaging, it is a reasonable approximation to neglect the inelastic and multiple scattering. In, for example, amorphous carbon and for this angle the partial cross section for elastic scattering [89] is a factor of 5 larger than the partial cross section for inelastic scattering.

For a scattering medium containing more than one type of atoms the average scattering cross section $\langle\sigma(\beta)\rangle$ has to be calculated, given by the sum of the $\sigma_i(\beta)$ for each atom multiplied by its composition fraction p_i (e.g., H_2O has $p_H = 2/3$, $p_O = 1/3$) [79,82]:

$$\langle\sigma(\beta)\rangle = \sum_i p_i \sigma_i(\beta) \quad (13.5)$$

In a first approximation $\langle\sigma(\beta)\rangle$ can also be calculated using a weighted quadratic average $\langle Z^2 \rangle^{1/2}$,

$$\langle Z^2 \rangle^{1/2} = \sqrt{\sum_i p_i Z_i^2} \quad (13.6)$$

The number of total atoms per unit volume is given by $\rho N_A/\langle W \rangle$, with the average molecular weight $\langle W \rangle$ obtained from:

$$\langle W \rangle = \sum_i p_i W_i \quad (13.7)$$

The amount of electrons elastically scattered by the sample N_{sample} into angle β is thus,

$$\frac{N_{\text{sample}}}{N_0} = 1 - \exp(-z\langle\sigma(\beta)\rangle\rho N_A/\langle W \rangle) = 1 - \exp\left(-\frac{z}{l_{\text{sample}}}\right) \quad (13.8)$$

with the free path length of the sample l_{sample} .

13.4.4 Detection of an Embedded Staining Particle

Conventional thin sections typically consist of an embedding medium with thickness T containing a biological structure outlined by the staining material. The calculations performed here are on a conventional thin section stained with osmium tetroxide and embedded in epoxy. Osmium tetroxide has the values $\rho = 5.1 \text{ g/cm}^3$, $\langle Z^2 \rangle^{1/2} = 34.7$, $\langle W \rangle = 50.8 \text{ g/mol}$, leading to $\langle l \rangle = 189 \text{ nm}$ ($\beta = 30 \text{ mrad}$). The parameters of epoxy are, $\rho = 1.3 \text{ g/cm}^3$, $\langle Z^2 \rangle^{1/2} = 4.8$, $\langle W \rangle = 7.5 \text{ g/mol}$ [82,116], leading to $\langle l \rangle = 4.03 \text{ }\mu\text{m}$. Small volumes of the staining material embedded in the section have to be detected (see Figure 13.10). When focusing the electron beam in a certain spot inside a certain volume of stain with thickness z and free path length l_{stain} , the signal N_{stain} in the ADF detector receives both the scattering by the staining particle and the scattering contribution from the medium with free path length l_{medium} through thickness $T - z$, resulting in N_{signal} electrons:

$$N_{\text{signal}} = N_0 \left\{ 1 - \exp \left(- \left[\frac{z}{l_{\text{stain}}} + \frac{T - z}{l_{\text{medium}}} \right] \right) \right\} \quad (13.9)$$

A few assumptions can be made. Typically $T = 100 \text{ nm}$, $z = 2 \text{ nm}$. It is, therefore, reasonable to assume that $T - z \cong T$ and that both z/l_{stain} and T/l_{medium} are small numbers, such that the first-order Taylor expansions can be used ($1 - \exp(-x) \cong x$) and thus,

$$N_{\text{signal}} \cong N_0 \left(\frac{z}{l_{\text{stain}}} + \frac{T}{l_{\text{medium}}} \right) \quad (13.10)$$

When the beam is shifted just outside the volume of material the detector receives only N_{bkg} background electrons from the contribution of the embedding medium with thickness T :

$$N_{\text{bkg}} = N_0 \left\{ 1 - \exp \left(- \frac{T}{l_{\text{medium}}} \right) \right\} \cong \frac{N_0 T}{l_{\text{medium}}} \quad (13.11)$$

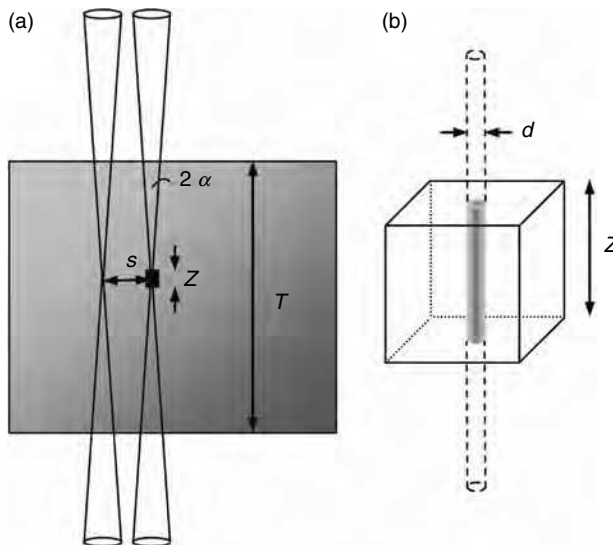


FIGURE 13.10 Principle of 3D detection of a staining particle. (a) Detection of a small volume of material with height z inside a matrix of embedding medium with thickness T . Two electron beams spaced by s are shown with beam semiangle α focused at the position of the sample. (b) Detection of a volume of material with cube length z using a beam with diameter d .

The scattering by the medium can be assumed to be approximately the same for all position of the beam in a sample with a uniform sample thickness and contributes to the background noise in the image only.

13.4.5 Confidence Level of Detection

To detect a staining particle of the size of a pixel the amount of electrons in the detector should be sufficient to reach the confidence level. Typically, the signal should be atleast a factor of $\chi = 3$ larger than the signal-to-noise ratio SNR [82,114,121]. Note that smaller values can be allowed when objects, for example lines, can be clearly recognized in the image [14]. Electron detection is typically limited by Poisson statistics with $SNR = \sqrt{n}$, with n the number of electrons arriving at the detector. For state-of-the-art detectors in the STEM, it can be assumed that additional noise can be neglected and that the collection efficiency approaches 100%. We can now write:

$$SNR = \frac{N_{\text{signal}} - N_{\text{bkg}}}{\sqrt{(N_{\text{signal}})^2 + (\sqrt{n_{\text{bkg}}})^2}} = \frac{N_0 z}{l_{\text{stain}}} \frac{1}{\sqrt{N_0 \left(\frac{z}{l_{\text{stain}}} + \frac{2T}{l_{\text{medium}}} \right)}} \quad (13.12)$$

Assuming $z/l_{\text{stain}} \ll T/l_{\text{medium}}$, one obtains:

$$SNR = \frac{z}{l_{\text{stain}}} \sqrt{\frac{N_0 l_{\text{medium}}}{T}} \quad (13.13)$$

13.4.6 Dose-Limited Resolution

The maximal number of available electrons is limited by radiation damage to the maximal dose $q = 4 \times 10^3 \text{ e}^-/\text{\AA}^2$. The highest current density is obtained at the focus and thus,

$$N_0 = qd^2 \quad (13.14)$$

The probe size d can generally be different from z . In the example of Figure 13.10, the cubic volume with edges z are imaged with an electron beam with probe size d smaller than z . In the lateral direction only a fraction of the volume interacts with the beam, whereas the beam interacts with the thickness z in the axial direction. The minimum value of z for detection is thus,

$$z = \frac{\chi l_{\text{stain}}}{d} \sqrt{\frac{T}{q l_{\text{medium}}}} \quad (13.15)$$

This equation gives the minimum height of a stain particle that can be detected given a certain probe size d . The scanning step size s can be made as small as the probe size to obtain high resolution in the lateral direction. This equation can be compared with an earlier relation to estimate the resolution δ as function of the dose [114], $\chi/\sqrt{(qC^2f)}$, with C^2f defining the contrast and the efficiency of the detection. For $d = 0.08 \text{ nm}$ and $T = 90 \text{ nm}$ Equation 11.15 gives $z = 1.7 \text{ nm}$. Thus, the STEM can detect staining particles with a dimension $0.08 \times 0.08 \times 1.7 \text{ nm}^3$, giving a volume resolution $\delta = 0.01 \text{ nm}^3$. From Equation 13.15 also follows that image processing, for example by shape recognition, directly leads to resolution improvement by lowering the value of χ .

The maximal dose of $4 \times 10^3 \text{ e}^-/\text{\AA}^2$ relates to homogeneous radiation in TEM imaging. The situation is different in STEM imaging with a small probe size and a large convergence angle. The maximal dose is only applied directly at the focus point, whereas adjacent volumes are irradiated with less current density. A large fraction of the sample volume is not irradiated at all for the case the images are recorded with d smaller than s . For example, with $d = 0.08 \text{ nm}$ and $s = 1 \text{ nm}$, only 1/156 fraction of the pixel surface at the focal point is irradiated. It can be debated that especially type I damage will be largely reduced when only a small volume is irradiated inside a much larger unirradiated volume. Moreover, the effects of type II damage will likely be restricted to the small-irradiated volume and not propagate through the whole sample. It was indeed reported that the critical dose in EELS experiments on polymers was increased by a factor of 10^2 – 10^4 when irradiating with a small spot [113,115]. Equation 13.15 for a dose limit of $4 \times 10^3 \text{ e}^-/\text{\AA}^2$ can thus be safely expected to represent the upper limit of the resolution.

13.4.7 Dose-Limited Resolution in Focal Series

A series of images has to be recorded at different focus values for 3D imaging. This set of images has to be recorded within the available dose. The question is how much dose the imaging of one slice contributes to the other slices. Several regimes of operation can be distinguished depending on the probe size d , on the lateral step size s of the scan, the focus difference between each slice h , and the number of recorded slices T/h . When $d = s$ the total dose $q \cong q_0 T/h$, with q_0 the dose of one slice. When $d \ll s$ the total dose can be much smaller. For a beam with spot size d in the focal plane the beam is approximately $d + 2h\alpha$ wide at the height h above and below the focal plane, and thus involves less current density. The imaging of one pixel in one slice, consequently, radiates the adjacent slices with a reduced dose. As the contribution to the total dose per slice will be the largest from its neighbors, the upper limit for the total dose is the dose of the central slice in the depth sequence:

$$q = 2q_0 \sum_{i=0}^{T/2h} \frac{d^2}{(d + 2ih\alpha)^2} \quad (13.16)$$

which is valid for $s \geq d + \alpha T$. Consider imaging a sample of 90 nm thickness with $d = 0.08 \text{ nm}$ and $\alpha = 23 \text{ mrad}$, such that $s = 2.1 \text{ nm}$. According to the Nyquist criterion the sampling frequency should be at least 2 times higher than the highest spatial frequency in the data [14]. The lateral resolution is thus 4 nm. For the axial resolution of the STEM of 7.4 nm, $h = 3.5 \text{ nm}$. The corresponding 26 exposures in focus steps of 3.5 nm give a total dose per slice that is only a factor of 2.4 larger than the dose needed to image one slice. The focus series will always be recorded with several slices above and below the sample, but their contribution to the dose can be neglected for these settings.

For $q = 2.4q_0$, the corresponding value of $z = 2.6 \text{ nm}$, a value slightly smaller than h . Thus, imaging can take place with an lateral resolution of 4 nm and an axial resolution of 7 nm. The volume resolution is 112 nm^3 .

The imaging can be optimized in a few ways. Firstly, some overlap of the imaging beams at the edges of the sample is not likely to lead the beam damage, i.e., s can be significantly smaller than calculated here. Secondly, the effect of beam damage of the imaging of one slice to the adjacent slices can be largely reduced by a simple trick. After the imaging of a slice, the probe is slightly shifted to reduce the overlap of irradiated areas of adjacent slices. Considering also that the actual radiation damage might be much less than expected for uniform radiation, it can be concluded that the resolution numbers presented here are upper estimates only. Still, the calculated lateral resolution is already beyond the resolution that a typical stained and embedded sample allows, as these samples often suffer from artifacts limiting the resolution in the image [25,122,123].

13.5 Initial Experimental Results on a Biological Sample

13.5.1 Focal Series of a Conventional Thin Section

To test the 3D STEM technique we have imaged a conventional thin section. 3T3 cells were stained with osmium tetroxide and lead citrate and embedded in epoxy (Embed-812) [116]. Small (15 nm) gold particles were put on both sides of the sample, and covered with a thin sheet of amorphous carbon (20 nm thickness). Figure 13.11 shows one image with a region inside a cell at the position of a Golgi apparatus. Numerous tubular, vesicular and saccular membranes with sharp structures can be seen. The Golgi apparatus itself appeared as a stack of saccules (i.e., cisternae). Each cisternae in the stack showed varying extents of fenestration, with the amount of fenestration decreasing *cis* to *trans* across the stack (black arrow). In the imaging procedure, the corrector was first aligned in an automated procedure while imaging the amorphous carbon film at the side of the section. Then, the section was searched for cells. At the position of a cell, the focus positions at the upper and the lower side of the sample were determined by imaging at a magnification of 20k and continuously changing the focus. Then a focal series was recorded at a magnification of 100k and with focal steps of 10 nm. A total of 40 frames was recorded at a beam current of about 50 pA, 512×512 pixel images with a pixel time of 32 μ s, leading to a total exposure time of 6 min in a vacuum of 5×10^{-9} torr. All slices of the focus series were normalized to the same mean intensity per slice and the noise in the slices was filtered using the convolution filter. The lateral drift during acquisition was ~ 4 nm, which was corrected for by aligning all slices with respect to the one in the middle of the stack using the Amira software Resolve RT 40 (Mercury Computer Systems). An overview image was recorded after the focal series, showing only minor change of the sample, some contamination buildup, and a slight deformation at the edges.

The thickness of the section was measured to be $0.21 + 0.02 \mu\text{m}$ by determining the *z*-positions, where the gold particles were in focus. Figure 13.11A shows several membranes of the Golgi apparatus. From the images of small line-shaped objects it was estimated that the lateral resolution was on the order of the pixel size, i.e., 2 nm. It can be seen that the image of one plane contains a significant amount of signal from the adjacent planes, leading to a blurring of the image. This effect is common in wide-field focal series recorded with an optical microscope and the image has to be deconvolved with the point spread function (PSF) [14].

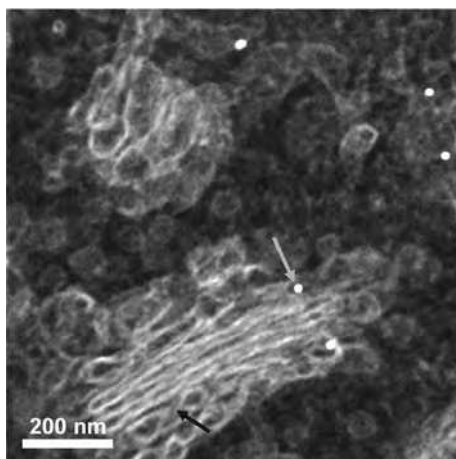


FIGURE 13.11 3D focal STEM series of a conventional thin section containing 3T3 (mouse fibroblast cell line) of $0.2 \mu\text{m}$ thickness at 300 kV and 23 mrad. Image of the Golgi apparatus focused at one side of the sample where the gold particle as pointed to with the arrow was in focus.

13.5.2 Deconvolution

An image I of an object O in the focal plane is blurred by the imaging instrument expressed by the integral [124]:

$$I(\mathbf{x}) = \int \text{PSF}(\mathbf{x} - \mathbf{y})O(\mathbf{y})d\mathbf{y} + N(\mathbf{x}) \quad (13.17)$$

Here, \mathbf{x} is a 3D vector and is convoluted with the $\text{PSF}(\mathbf{x}-\mathbf{y})$, assuming that the PSF is the same for each pixel in the image. The imaging process also adds noise $N(\mathbf{x})$. For an ideal image, i.e., without noise, the convolution can be rewritten in Fourier space by the wave vectors \mathbf{k} and the simple algebraic product:

$$\tilde{I}(\mathbf{k}) = \tilde{\text{PSF}}(\mathbf{k})\tilde{O}(\mathbf{k}) \quad (13.18)$$

The image reconstruction will then be solved in Fourier space:

$$\tilde{O}(\mathbf{k}) = \tilde{I}(\mathbf{k})/\tilde{\text{PSF}}(\mathbf{k}) \quad (13.19)$$

Several deconvolution algorithms, for example the iterative maximum-likelihood image restoration, exist to deconvolve a real image with noise [14,17,124]. The PSF can be determined by calculation, but this often leads to errors due to uncertainties in several of the optical parameters. Another way is to record images of strongly scattering objects that are smaller than the probe size, which then directly represent the PSF [14,17]. For the probe size of the electron microscope (~ 0.1 nm) this would mean recording images of single atoms with high Z . Imaging with such high resolution was not possible with the stained sample of 200 nm thickness.

Alternatively, the PSF can be determined from the image of an object of a known shape,

$$\tilde{\text{PSF}}(\mathbf{k}) = \tilde{I}(\mathbf{k})/\tilde{O}(\mathbf{k}) \quad (13.20)$$

We have used the gold particle in Figure 13.11 as a test object. The image of the object in focus was assumed to reflect the correct lateral shape of the object. Convolution of the probe with the object in the lateral direction in the focal plane was neglected. We have assumed that the object was 10 nm thick or less, such that in the focal series recorded with focus steps of 10 nm it is only in focus in one frame.

We have used Amira software ResolveRT 4.0 to perform the deconvolution. First, the object was defined by selecting a 16×16 pixel image around the gold particle from the frame where it was in focus. Second, 3D image was selected from the focal series around the gold particle. The image and the object were deconvolved to obtain the PSF. In the last step, the full image was deconvolved with the PSF. The focus positions of the gold particles were used to check the validity of the deconvolution.

13.5.3 Deconvolved Images

Data from the deconvolved 3D data set are shown in Figure 13.12. To visualize the 3D sensitivity we have zoomed-in on the data set at the position of about the middle of the Golgi stack as shown in Figure 13.11. Figure 13.12a shows an image from the original (before deconvolution) data set at the same focus position as Figure 13.12c. Three of the deconvolved images are shown in Figure 13.12b–d; each image differing 50 nm in the focus position. The deblurring effect of the deconvolution is clearly visible, similar to that found with deconvolution in wide field light microscopy [14]. Between the images of Figure 13.12b–d, numerous changes in the structures of the membranes and filamentous structures within the Golgi stack can be seen. Several oval dashed lines with different colors are added as a guide to the eye to compare the same structures in each image. The positions were chosen arbitrarily to provide a few examples of structural changes as a function of the focus position. For example, in the top oval in

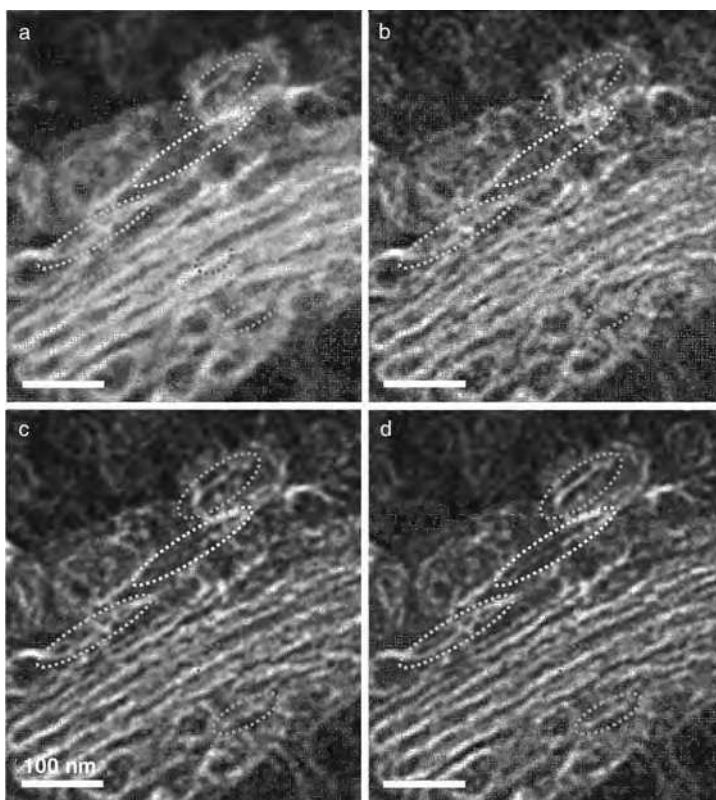


FIGURE 13.12 Deconvolved 3D STEM images of a conventional thin section. (a) Original (before deconvolution) image at the same focus position as image (c). (b)–(d) Images of the deconvolved data set each differing 50 nm in focus position. The oval dashed lines are added to guide the eye.

Figure 13.12d we can see a continuous line (a membrane structure) that becomes interrupted going through Figure 13.12c and b. In the oval second from the top, a tubular shape is visible in Figure 13.12d, which disappears in Figure 13.12c and a different structure is visible in Figure 13.12b. In the bottom oval an opening between two structures is visible in Figure 13.12c, while it is closed in Figure 13.12d. In the remaining three ovals similar changes can be observed and various changes can be discerned at other positions.

This data thus provides the first proof that 3D STEM can be applied successfully to biological samples with a depth resolution much smaller than the sample thickness. We conclude also that deconvolution can be used to enhance the 3D resolution. More accurate deconvolution procedures could be developed to take account of the variation of the PSF with the focus position, which would allow a higher depth resolution in the 3D reconstruction.

13.6 Future Outlook

We expect that the deconvolution can be improved, by providing better estimates of the noise statistics, testing several deconvolution algorithms [124], accounting for the variation of the PSF with the depth in the sample and determining the PSF in a more accurate way on much smaller particles than used here. The optimal imaging conditions have to be found, aided by further model optimization. These optimizations could possibly lead to a better resolution than calculated here, as was demonstrated to be possible in light optics [10,17]. The model calculations presented here give some idea of the parameter space to be explored for optimal imaging. A detailed model of the 3D resolution should

also include different contrast mechanisms and the effect of beam blurring on the resolution, such that the imaging of unstained samples and the imaging of thicker sections can be described as well. The model should be tested rigorously on a variety of samples. The detection efficiency can possibly be improved by an optimized combination of detector signals, as was demonstrated for STEM imaging by Colliex et al. [82] in a different context, resulting in an improvement of the resolution. A major step would be to develop a liquid nitrogen holder with sufficient stability for the aberration-corrected STEM, such that cryo-3D STEM could be performed. The depth resolution will improve for the larger opening angles of a second generation of aberration correctors compensating all geometric aberrations up to fifth order, which will enable opening angles of 50 mrad and 1 nm depth resolution. High-*Z* markers, for example gold particles, can be added to visualize certain processes in the cell [72]. The position of these particles could be determined with subnanometer resolution in both lateral and axial directions. Finally, the STEM can possibly be used to image proteins and cells directly in their natural, wet environment by employing a liquid cell [125]. We envision that eventually it will be feasible to perform time-resolved 3D in situ microscopy of biological samples with a resolution of a few nanometers.

13.7 Comparison of 3D STEM with TEM Tomography for Biology

3D STEM is a 3D technique for the imaging of whole assemblies, as is tilt-series TEM, in contrast to the averaging techniques using diffraction from crystals or multiple images of identical objects. The resolution of the tomogram obtained in a tilt series (both on cryo and embedded or stained) is typically 5–10 nm in *xyz* [36–40]. From our calculations it follows that 3D STEM with the present microscopes already has approximately the same resolution ($4 \times 4 \times 7$ nm) on a conventional thin section. Improvement of the resolution is expected to be possible with a dedicated deconvolution procedure and with a new generation of aberration corrected microscopes.

The second advantage will be provided by the speed of the imaging technique. A focal series is readily recorded in 5 min, without need for realignment or adjustment of the microscope. TEM tomography, even automated [126,127], is still a delicate technique where manual alignment on markers added on the sides of the sample is often required. The sample does not have to be tilted such that larger and thicker samples can be imaged without suffering from beam blurring and focusing issues. Moreover, the absence of a tilt series reduces the drift alignment and magnification correction. 3D STEM could also be acquired at several tilt angles, combining the advantages of both techniques. The data acquisition is not limited to a data set representing a cubic volume, but 3D STEM can in principle acquire a data set of any shape. For example, a long and thin object, such as an axon, could readily be captured with only a minimum number of surrounding pixels using selected scanning of the electron beam. As a result, objects with elongated shapes would be captured as a whole within a data set of reduced size.

13.8 Conclusions

Aberration-corrected STEM opens a new perspective for EM of biological samples. We have presented initial calculations that suggest 3D STEM can potentially become a future alternative to TEM tomography for conventional thin sections. The first experiments have demonstrated the feasibility of the technique, but further experiments are needed to explore the maximal resolution. 3D STEM has several other advantages over TEM tomography due to the absence of mechanical tilt requirements.

Acknowledgments

We are grateful to J. Lippincott-Schwartz for support, K. van Benthem for discussions, and W.H. Sides Jr., for experimental help. This research was sponsored by the Division of Materials Sciences and

Engineering, Office of Basic Energy Sciences, U.S. Department of Energy, under contract DE-AC05-00OR22725 with Oak Ridge National Laboratory, managed and operated by UT-Battelle, LLC.

References

1. McPherson, J., et al. 2001. A physical map of the human genome. *Nature* 409:934–941.
2. Sachidanandam, R., et al. 2001. A map of human genome sequence variation containing 1.42 million single nucleotide polymorphisms. *Nature* 409:928–933.
3. Venter, J.C., et al. 2001. The sequence of the human genome. *Science* 291:1304–1351.
4. Sali, A.R., T. Earnest, and W. Baumeister. 2003. From words to literature in structural proteomics. *Nature* 422:216–225.
5. Bryson, J.W., S.F. Betz, H.S. Lu, D.J. Suich, H.X. Zhou, K.T. O’Neil, and W.F. DeGrado. 1995. Protein design, a hierarchic approach, *Science* 270:935–941.
6. Ali, M.A., E. Peisach, K.N. Allen, and B. Imperialli. 2004. X-ray structure analysis of a designed oligomeric miniprotein reveals a discrete quaternary architecture. *Proc Natl Acad Sci* 101(33):12183–12188.
7. Rau, H.K., N. de Jonge, and W. Haehnel. 1998. Modular synthesis of *de novo*-designed metalloproteins for light-induced electron transfer. *Proc Natl Acad Sci* 95:11526–11531.
8. Sali, A. 1998. 100,000 protein structures for the biologist. *Nat Struct Biol* 5:1029–1032.
9. Frank, J. 2006. *Three-dimensional electron microscopy of macromolecular assemblies—Visualization of biological molecules in their native state*. Oxford: Oxford University Press.
10. Westphal, V., and S.W. Hell. 2005. Nanoscale resolution in the focal plane of an optical microscope. *Phys Rev Lett* 94:143903–/–4.
11. Nellist, P.D., et al. 2004. Direct sub-angstrom imaging of a crystal lattice. *Science* 305:1741.
12. van Benthem, K., et al. 2005. Three-dimensional imaging of individual hafnium atoms inside a semiconductor device. *Appl Phys Lett* 87:034104-1-3.
13. Borisevich, A.Y., A.R. Lupini, and S.J. Pennycook. 2006. Depth sectioning with the aberration-corrected scanning transmission electron microscope. *Proc Natl Acad Sci* 103(9):3044–3048.
14. Pawley, J.B. 1995. *Handbook of biological confocal microscopy*, 2nd ed. New York: Springer.
15. Schrader, M., S.W. Hell, and H.T.M. van der Voort. 1996. Potential of confocal microscopes to resolve in the 50–100 nm range. *Appl Phys Lett* 69:3644–3646.
16. Lippincott-Schwartz, J., E. Snapp, and A. Kenworthy. 2001. Studying protein dynamics in living cells. *Nat Rev* 2:444–456.
17. Carrington, W.A., R.M. Lynch, E.D.W. Moore, G. Isenberg, K.E. Fogarty, and F.S. Fay. 1995. Superresolution three-dimensional images of fluorescence in cells with minimal light exposure. *Science* 268:1483–1487.
18. Abbe, E. 1873. Beiträge zur theorie des mikroskops und der mikroskopischen wahrnehmung. *Archiv für Mikroskopische Anatomie und Entwicklungsmechanik* 9:413–468.
19. Schrader, M., S.W. Hell, and H.T.M. van der Voort. Three-dimensional super-resolution with a 4Pi-confocal microscope using image restoration. *J Appl Phys* 84:4033–4042.
20. Ferreira, K.N., T.M. Iverson, K. Maghlaoui, J. Barber, and S. Iwata. 2004. Architecture of the photosynthetic oxygen-evolving center. *Science* 303:1831–1838.
21. Fiaux, J., E.B. Bertelsen, A.L. Horwich, and K. Wuethrich. 2002. NMR analysis of a 900 K GroEL–GroES complex. *Nature* 418:207–211.
22. Gutberlet, T., U. Heinemann, and M. Steiner. 2001. Protein crystallography with neutrons—Status and perspectives. *Acta Crystallogr D* 57:349–354.
23. Meyer-Ilse, W. et al. 2001. High resolution protein localization using soft x-ray microscopy. *J. Micr.* 201:395–403.
24. Bahatyrova, S., et al. 2004. The native architecture of a photosynthetic membrane. *Nature* 430:1058.

25. Lucic, V., F. Foerster, and W. Baumeister. 2005. Structural studies by electron tomography: From cells to molecules. *Annu Rev Biochem* 74:833–865.
26. McIntosh, J.R., D. Nicastro, and D.N. Mastrorade. 2005. New views of cells in 3D: An introduction to electron tomography. *Trends Cell Biol* 15:43–51.
27. van Heel, M., et al. 2000. Single-particle electron cryo-microscopy towards atomic resolution. *Q Rev Biophys* 33:307–369.
28. de Rosier, D.J., and A. Klug. 1968. Reconstruction of three dimensional structures from electron micrographs. *Nature* 217:130–134.
29. Henderson, R., and P.N.T. Unwin. 1975. Three-dimensional model of purple membrane obtained by electron microscopy. *Nature* 257:28–32.
30. Klug, A. 1982. From macromolecules to biological assemblies, Nobel Lecture.
31. Bozzola, J.J., and L.D. Russell. 1992. *Electron microscopy*. Boston: Jones & Bartlett Publishers.
32. Taylor, K.A., and R.M. Glaeser. Electron microscopy of frozen hydrated biological specimens. *J Ultrastruct Res* 55:448–456.
33. De Carlo, S., C. El-Bez, C. Alvarez-Rua, J. Borge, and J. Dubochet. 2002. Cryo-negative staining reduces electron-beam sensitivity of vitrified biological particles. *J Struct Biol* 138:216–226.
34. Frank, J. 1992. *Electron tomography, three-dimensional imaging with the transmission electron microscope*. New York: Plenum Press.
35. Subramaniam, S., and J.L.S. Milne. 2004. Three-dimensional electron microscopy at molecular resolution. *Annu Rev Biophys Biomol Struct* 33:141–155.
36. Unser, M. et al. 2005. Spectral signal-to-noise ratio and resolution assessment of 3D reconstructions. *J Struct Biol* 149:243–255.
37. Cardonne, G., K. Gruenewald, and A.C. Steven. 2005. A resolution criterion for electron tomography based on cross-validation. *J Struct Biol* 151:117–129.
38. McEwen, B.F., M. Marko, C.E. Hsieh, and C. Mannella. 2002. Use of frozen hydrated axonemes to assess imaging parameters and resolution limits in cryoelectron tomography. *J Struct Biol* 138:47–57.
39. Iancu, C.V., E.R. Wright, J.B. Heymann, and G.J. Jensen. 2006. A comparison of liquid nitrogen and liquid helium as cryogens for electron cryotomography. *J Struct Biol* 153:231–240.
40. Hsieh, C.E., A. Leith, C.A. Mannella, J. Frank, and M. Marko. 2006. Towards high-resolution three-dimensional imaging of native mammalian tissue: Electron tomography of frozen-hydrated rat liver sections. *J Struct Biol* 153:1–13.
41. Medalia, O., I. Weber, A.S. Frangakis, D. Nicastro, G. Gerisch, and W. Baumeister. 2002. Macromolecular architecture in eukaryotic cells visualized by cryoelectron tomography. *Science* 298:1209–1213.
42. Bouwer, J.C., et al. 2004. Automated most-probably loss tomography of thick selectively stained biological specimens with quantitative measurement of resolution improvement. *J Struct Biol* 148:297–306.
43. Colliex, C., C. Mory, A.L. Olins, D.E. Olins, and D.E. Tence. 1989. Energy filtered STEM imaging of thick biological sections. *J Microsc* 153:1–21.
44. Liu, J., D.W. Taylor, and K.A. Taylor. 2004. A 3-D reconstruction of smooth muscle alpha-actinin by cryoEM reveals two different conformations at the actin-binding region. *J Mol Biol* 338:115–125.
45. Mogelsvang, S., B.J. Marsh, M.S. Ladinsky, and K.E. Howell. 2004. Predicting function from structure: 3D structure studies of the mammalian Golgi complex. *Traffic* 5:338–345.
46. Beck, M., et al. 2004. Nuclear pore complex structure and dynamics revealed by cryoelectron tomography. *Science* 306:1387–1390.
47. Henderson, R., J.M. Baldwin, T.A. Ceska, F. Zemlin, E. Beckmann, and K.H. Downing. 1990. Model for the structure of bacteriorhodopsin on high-resolution electron cryo-microscopy. *J Mol Biol* 213:899–929.

48. Murata, K., et al. 2000. Structural determinants of water permeation through aquaporin-1. *Nature* 407:599–605.
49. Kuehlbrandt, W., D.N. Wang, and Y. Fujiyoshi. 1994. Atomic model of plant light-harvesting complex by electron crystallography. *Nature* 367:614–621.
50. Zhang, P., C. Toyoshima, K. Yonekura, N.M. Green, and D.L. Stokes. 1998. Structure of the calcium pump from sarcoplasmic reticulum at 8-Å resolution. *Nature* 392:835–839.
51. Li, H., D.J. De Rosier, W.V. Nicholson, E. Nogales, and K.H. Downing. 2002. Microtubule structure at 8 Å resolution. *Structure* 10:1317–1328.
52. Zhang, X., Y. Ji, L. Zhang, S.C. Harrison, D.C. Marinescu, M.L. Nibert, and T.S. Baker. 2005. Features of reovirus outer capsid protein $\mu 1$ revealed by electron cryomicroscopy and image reconstruction of the virion at 7.0 Å resolution. *Structure* 13:1545–1557.
53. Jiang, W., and S.J. Ludtke. 2005. Electron cryomicroscopy of single particles at subnanometer resolution. *Curr Opin Struct Biol* 15:571–577.
54. Ruska, E. 1934. On progress in the construction and performance of the magnetic electron microscope. *Z Phys* 87:580–602.
55. Knoll, M., and E. Ruska. 1932. The electron microscope. *Z Phys* 78:318–339.
56. Ruska, E. 1986. The development of the electron microscope and of electron microscopy, Nobel Lecture.
57. Kruger, D.H., P. Schneck, and H.R. Gelderblom. 2000. Helmut Ruska and the visualization of viruses. *Lancet* 355:1713–1717.
58. von Ardenne, M. 1938. Das Elektronen-Rastermikroskop. Theoretische Grundlagen. *Z Phys* 109:553–572.
59. Crewe, A.V., J. Wall, and J. Langmore. 1970. Visibility of single atoms. *Science* 168:1338–1340.
60. Crewe, A.V., and J.A. Wall. 1970. A scanning microscope with 5 Å resolution. *J Mol Biol* 48:375–393.
61. Fowler, R.H., and L. Nordheim. 1928. Electron emission in intense electric fields. *Proc Roy Soc London A* 119:173–181.
62. Good, R.H., and E.W. Mueller. 1956. Field emission, in *Handbuch der Physik*, XXI, Fluegge, S. Springer verlag, Berlin, pp. 176–231.
63. Crewe, A.V. 1971. High resolution scanning microscopy of biological specimens. *Phil Trans Roy Soc London B* 261:61–70.
64. Henkelman, R.M., and F.P. Ottensmeyer. 1971. Visualization of single heavy atoms by dark field electron microscopy. *Proc Natl Acad Sci* 68:3000–3004.
65. Wall, J., J. Langmore, M. Isaacson, and A.V. Crewe. 1974. Scanning transmission electron microscopy at high resolution. *Proc Natl Acad Sci* 71:1–5.
66. Ottensmeyer, F.P., R.F. Whiting, and A.P. Korn. 1975. 3-Dimensional structure of herring sperm protamine Y-I with aid of dark field electron-microscopy. *Proc Natl Acad Sci* 72:4953–4955.
67. Kapp, O.H., M.G. Mainwaring, S.N. Vinogradov, and A.V. Crewe. Scanning-transmission electron-microscopic examination of the hexagonal bilayer structures formed by the reassociation of 3 of the 4 subunits of the extracellular hemoglobin of lumbricus-terrestris. *Proc Natl Acad Sci* 84 (21):7532–7536.
68. Yuan, J.F.B., D.R. C.G., and F.P. Ottensmeyer. 2005. 3D reconstruction of the Mu transposase and the Type 1 transpososome: a structural framework for Mu DNA transposition. *Genes & Development* 19:840–852.
69. Midgley, P.A., M. Weyland, J.M. Thomas, and B.F.G. Johnson. 2001. Z-Contrast tomography: a technique in three-dimensional nanostructural analysis based on Rutherford scattering. *Chem-Comm* 18:907–908.
70. Kuebel, C., et al. 2005. Recent advances in electron tomography: TEM and HAADF-STEM tomography for materials science and semiconductor applications. *Microscopy and Microanalysis* 11:378–400.
71. Ohtsuki, M., M.S. Isaacson, and A.V. Crewe. 1979. Dark field imaging of biological macromolecules with the scanning-transmission electron-microscope. *Proc Natl Acad Sci* 76:1228–1232.

72. Xiao, Y., F. Patolsky, E. Katz, J.F. Hainfeld, and I. Willner. 2003. "Plugging into enzymes": nanowiring of redox enzymes by a gold nanoparticle. *Science* 299:1877–1881.
73. Treacy, M.M. J., A. Howie, and S.J.Z. Pennycook. 1980. Z contrast of supported catalyst particles on the STEM. *Electron Microscopy and Analysis* 1979:261–264.
74. Pennycook, S.J., S.D. Berger, and R.J. Culbertson. 1986. Elemental mapping with elastically scattered electrons. *J Microscopy* 144:229–249.
75. Ottensmeyer, F.P., E.E. Schmidt, and A.J. Olbrecht. 1973. Image of a sulfur atom. *Science* 179:175–176.
76. Ottensmeyer, F.P., D.P. Bazettjones, R.M. Henkelman, A.P. Korn, and R.F. Whiting. 1979. Imaging of atoms—Its application to the structure determination of biological macromolecules. *Chem Script* 14:257–262.
77. Ohtsuki, M., and A.V. Crewe. 1980. Optimal imaging techniques in the scanning-transmission electron-microscope—Applications to biological macromolecules. *Proc Natl Acad Sci* 77:4051–4054.
78. Langmore, J.P., J. Wall, and M.S. Isaacson. 1973. Collection of scattered electrons in dark field electron-microscopy.1. Elastic-scattering. *Optik* 38:335–350.
79. Engel, A. 1978. Molecular weight determination by scanning transmission electron microscopy. *Ultramicroscopy* 3:273–281.
80. Engel, A., W. Baumeister, and W.O. Saxton. 1982. Mass mapping of a protein complex with the scanning transmission electron microscope. *Proc Natl Acad Sci* 79:4050–4054.
81. Mastrangelo, I.A., P.V.C. Hough, V.G. Wilson, J.S. Wall, J.F. Hainfeld, and P. Tegtmeier. 1985. Monomers through trimers of large tumor antigen bind in region I and monomers through tetramers bind in region II of simian virus 40 origin of replication DNA as stable structures in solution. *Proc Natl Acad Sci* 82:3626–3630.
82. Colliex, C., C. Jeanguillaume, and C. Mory. 1984. Unconventional modes for STEM imaging of biological structures. *J Ultrastruct Res* 88:177–206.
83. Haider, M. 1989. Filtered dark-field and pure Z-contrast: Two novel imaging modes in a scanning transmission electron microscope. *Ultramicroscopy* 28:240–247.
84. Browning, N.D., M.F. Chisholm, and S.J. Pennycook. 1993. Atomic-resolution chemical-analysis using a scanning transmission electron microscope. *Nature* 366:143–146.
85. Varela, M., et al. 2005. Materials characterization in the aberration-corrected scanning transmission electron microscope. *Annu Rev Mater Res* 35:539–569.
86. Cowley, J.M. 1969. Image contrast in a transmission scanning electron microscope. *Apl Phys Lett* 15:58–59.
87. Engel, A., J.W. Wiggins, and D.C. Woodruff. 1974. Comparison of calculated images generated by 6 modes of transmission electron-microscopy. *J Appl Phys* 45:2739–2747.
88. Zeitler, E., and M.G.R. Thomson. 1970. Scanning transmission electron microscopy.1. *Optik* 31:258–280.
89. Reimer, L. 1984. *Transmission electron microscopy*. Springer, Heidelberg.
90. Spence, J.C.H. 2003. *High-resolution electron microscopy*, 3rd ed. Oxford University Press, Oxford.
91. Iijima, S. 1977. Observation of single and clusters of atoms in bright field electron-microscopy. *Optik* 48:193–214.
92. Ottensmeyer, F.P. 1982. Scattered electrons in microscopy and microanalysis. *Science* 215:461–466.
93. Schultheiss, K., F. Perez-Willard, B. Barton, D. Gerthsen, and R.R. Schroeder. 2006. Fabrication of a Boersch phase plate for phase contrast imaging in a transmission electron microscope. *Rev Sci Instr* 77:33701-1-4.
94. Pennycook, S.J., and L.A. Boatner. Chemically sensitive structure-imaging with a scanning transmission electron microscope. *Nature* 336:565–567.
95. Pennycook, S.J., and D.E. Jesson. 1990. High-resolution incoherent imaging of crystals. *Phys Rev Lett* 64:938–941.

96. Pennycook, S.J., and D.E. Jesson. 1991. High-resolution Z-contrast imaging of crystals. *Ultramicroscopy* 37:14–38.
97. Scherzer, O. 1936. Über einige Fehler von Elektronenlinsen. *Zeit Phys* 101:593–603.
98. Scherzer, O. 1947. Sparische und Chromatische Korrektur von Elektronen-Linsen. *Optik* 2:114–132.
99. Haider, M., S. Uhlemann, E. Schwan, H. Rose, B. Kabius, and K. Urban. 1998. Electron microscopy image enhanced. *Nature* 392:768–769.
100. Krivanek, O.L., N. Dellby, and A.R. Lupini. 1999. Towards sub-angstrom electron beams. *Ultramicroscopy* 78:1–11.
101. Bleloch, A., and A. Lupini. 2004. Imaging at the Picoscale. *Materials Today* 7:42–48.
102. Hawkes, P.W., and E. Kasper. 1989. *Principles of Electron Optics*. Academic Press.
103. Koops, H. 1978. Test of a chromatically corrected objective lens of an electron-microscope. *Optik* 52:1–18.
104. Dellby, N., O.L. Krivanek, P.D. Nellist, P.E. Batson, and A. Lupini. 2001. Progress in aberration-corrected scanning transmission electron microscopy. *J Elect Microsc* 50:177–185.
105. Rose, H. 1994. Correction of aberrations, a promising means for improving the spatial and energy resolution of energy-filtering electron-microscopes. *Ultramicroscopy* 56:11–25.
106. Beck, V.D. 1979. Hexapole spherical-aberration corrector. *Optik* 53:241–255.
107. Crewe, A.V., and D. Kopf. 1980. Sextupole system for the correction of spherical-aberration 55:1–10.
108. Shao, Z.F. 1988. On the 5th order aberration in a sextupole corrected probe forming system. *Rev Sci Instr* 59:2429–2437.
109. Krivanek, O.L. 1976. Method for determining coefficient of spherical aberration from a single electron micrograph. *Optik* 45:97–101.
110. Haider, M., S. Uhlemann, and J. Zach. 2000. Upper limits for the residual aberrations of a high-resolution aberration-corrected STEM. *Ultramicroscopy* 81:163–175.
111. Zaluzec, N.J. 2003. The scanning confocal electron microscope. *Microscopy Today* 6:8–11.
112. Hoppe, W. 1972. Drei-dimensionale abbildende elektronenmikroskope. *Z Naturforsch* 27a:919–929.
113. Egerton, R.F., P. Li, and M. Malac. 2004. Radiation damage in the TEM and SEM. *Micron* 35:399–409.
114. Isaacson, M., D. Johnson, and A.V. Crewe. 1973. Electron beam excitation and damage of biological molecules; its implications for specimen damage in electron microscopy. *Rad Res* 55:205–224.
115. Varlot, K., J.M. Martin, C. Quet, and Y. Kihn. 1997. Towards sub-nanometer scale EELS analysis of polymers in the TEM. *Ultramicroscopy* 68:123–133.
116. Glauert, A.M., and P.R. Lewis. 1998. *Biological specimen preparation for transmission electron microscopy*. Portland Press, London.
117. Luther, P.K., M.C. Lawrence, and R.A. Crowther. 1988. A method for monitoring the collapse of plastic sections as a function of electron dose. *Ultramicroscopy* 24:7–18.
118. Goldstein, J.I. 1979. Principles of thin film x-ray microanalysis, in *Introduction to analytical electron microscopy*, Hren, J.J., Goldstein, J.I., and Joy, D.C. Plenum Press, New York, pp. 83–120.
119. Joy, D.C. 1995. *Monte Carlo Modeling for Electron Microscopy and Microanalysis*. Oxford University Press, New York.
120. Williams, D.B., J.R. Michael, J.I. Goldstein, and A.D. Romig Jr. Definition of the spatial resolution of x-ray microanalysis in thin foils. *Ultramicroscopy* 47:121–132.
121. Rose, A. 1948. Television pickup tubes and the problem of noise. *Adv Electron* 1:131–166.
122. Kellenberger, E., R. Johansen, M. Maeder, B. Bohrmann, E. Stauffer, and W. Villiger. 1992. Artefacts and morphological changes during chemical fixation. *J Microsc* 168:181–201.
123. Hayat, M.A. 2000. *Principles and techniques of electron microscopy: Biological applications*. Cambridge University Press, Cambridge.

124. Puetter, R.C., T.R. Gosnell, and A. Yahil. 2005. Digital image reconstruction: deblurring and denoising. *Annu Rev Astron Astrophys* 43:139–194.
125. Thiberge, S., O. Zik, and E. Moses. 2004. An apparatus for imaging liquids, cells, and other wet samples in the scanning electron microscopy. *Rev Sci Instr* 75:2280.
126. Koster, A.J., H. Chen, J.W. Sedat, and D.A. Agard. 1992. Automated microscopy for electron tomography. *Ultramicroscopy* 46:207–227.
127. Mastronarde, D.N. 2005. Automated electron microscope tomography using robust prediction of specimen movements. *J Struct Biol* 152:36–51.

